GEOPHYSICS

A two-billion-year history for the lunar dynamo

Sonia M. Tikoo,[1,2,3,4]* Benjamin P. Weiss,[1,2] David L. Shuster,[2,3] Clément Suavet,[1] Huapei Wang,[1] Timothy L. Grove[1]

Magnetic studies of lunar rocks indicate that the Moon generated a core dynamo with surface field intensities of ~20 to 110 μT between at least 4.25 and 3.56 billion years ago (Ga). The field subsequently declined to <~4 μT by 3.19 Ga, but it has been unclear whether the dynamo had terminated by this time or just greatly weakened in intensity. We present analyses that demonstrate that the melt glass matrix of a young regolith breccia was magnetized in a ~5 ± 2 μT dynamo field at ~1 to ~2.5 Ga. These data extend the known lifetime of the lunar dynamo by at least 1 billion years. Such a protracted history requires an extraordinarily long-lived power source like core crystallization or precession. No single dynamo mechanism proposed thus far can explain the strong fields inferred for the period before 3.56 Ga while also allowing the dynamo to persist in such a weakened state beyond ~2.5 Ga. Therefore, our results suggest that the dynamo was powered by at least two distinct mechanisms operating during early and late lunar history.

INTRODUCTION

The Moon is a unique venue for exploring the longevity of dynamos generated by planetary bodies intermediate in size between planets and asteroids. A central conundrum is that the lunar dynamo was apparently intense and long-lived, with surface fields reaching ~20 to 110 μT between at least 4.25 and 3.56 billion years ago (Ga) (*1*–*6*). The field intensity then precipitously declined by at least an order of magnitude (possibly even to zero) by ~3.19 Ga (*7*–*9*). It is unknown whether this decrease reflects total cessation of the dynamo or whether the dynamo persisted beyond 3.56 Ga in a markedly weakened state.

The mechanisms that generated such a long-lived dynamo are uncertain but may include thermal convection (*10*–*13*) and mechanical stirring produced by differential rotation between the lunar core and mantle driven by impacts (*14*) or mantle precession (*15*, *16*). Geophysical evidence for a ~200- to ~280-km-radius solid inner core (*17*, *18*) within a larger ~220- to ~450-km-radius liquid outer core (*17*–*23*) also suggests that thermochemical convection resulting from core crystallization—the driving force behind the Earth's dynamo—may have helped sustain the dynamo (*24*–*26*). Without invoking special conditions, such as an early thermal blanket enveloping the lunar core, a hydrous lunar mantle, or a low core adiabatic heat flux, purely thermal convection dynamos are unlikely to persist beyond ~4 Ga (*6*). Impact-driven dynamos are transient [lasting up to a few thousand years after each large basin-forming impact (*14*)] and cannot have occurred after the last basin-forming impact at ~3.7 Ga (*5*). On the other hand, mantle precession or thermochemical convection may be capable of powering a dynamo well beyond 3.5 Ga (*6*).

Key to distinguishing between these lunar dynamo mechanisms is establishing the lifetime of the dynamo. However, the poor magnetic recording properties (*7*, *8*, *27*) and complex thermal and deformational histories of most lunar samples (*6*, *7*) as well as the rarity of young (<3.2 Ga) Apollo igneous samples have thus far hindered efforts to establish when the dynamo ultimately ceased. Although some Apollo-era studies have suggested that lunar samples as young as ~200 million years old (Ma) formed in lunar paleofields of ~1 to ~10 μT (*28*), most of these values are likely upper limits given the samples' magnetic recording fidelities (*8*, *27*, *29*). Furthermore, it has been proposed that impact-generated plasmas could generate transient magnetic fields [lasting up to ~1 day for large basin-forming impacts (*30*) or <~1 s for the small impacts after 3.7 Ga (*8*)] that could magnetize shocked and quickly cooled rocks throughout lunar history (*31*, *32*). Given these complexities, determining when the lunar dynamo actually ceased requires a young rock with exceptionally high-fidelity magnetic recording properties and a well-constrained thermal and shock history. To address these deficiencies, we conducted a new analysis of such a young lunar sample, glassy regolith breccia 15498.

Apollo 15 sample 15498 was collected on 1 August 1971 as unoriented float on the southern rim of Dune Crater within eastern Mare Imbrium. The rock consists of a cohesive impact melt glass matrix containing <1-mm- to ~2-cm-diameter mare basalt clasts (Fig. 1) (*33*, *34*). The clasts are petrogenetically related to the Apollo 15 quartz- and olivine-normative mare basalt suites, suggesting that the breccia was melted and assembled in close proximity to the Apollo 15 landing site (*35*). The rock is partially coated by a variably ~1- to 6-mm-thick spatter of impact melt glass (textural relationships indicate that this rind is younger than the interior breccia, but its precise age is unknown). A network of fissures lined with vesicular glass crosscuts the interior of the rock (see section S1). Although the basalt clasts contain abundant shock deformation features, including maskelynite (*33*, *34*), the lack of microfractures within the glassy matrix (see section S1) indicates that the rock has not been significantly shocked [peak pressures likely <~3 GPa (*36*)] since lithification.

The petrography and degree of crystallinity of the glassy matrix of 15498 suggest that it formed by viscous sintering of a clast-laden melt (*37*). During this primary cooling, ferromagnetic metal grains crystallized from the melt portion of the breccia. Consistent with a previous study of metal compositions in 15498 (*38*), our electron microprobe analyses found that the major ferromagnetic minerals within the resulting glass matrix are kamacite (α-$Fe_{1-x}Ni_x$ for x < ~0.05) and martensite (α_2-$Fe_{1-x}Ni_x$ for ~0.05 < x < ~0.19). If an ambient magnetic field was present at the time 15498 formed, kamacite and martensite grains with the observed compositions would have acquired mostly thermoremanent magnetization (TRM), with some possible contribution of thermochemical remanent magnetization (TCRM) during primary cooling on the Moon.

[1]Department of Earth, Atmospheric, and Planetary Sciences, Massachusetts Institute of Technology, 77 Massachusetts Avenue, Cambridge, MA 02139, USA. [2]Department of Earth and Planetary Science, University of California, Berkeley, Berkeley, CA 94720, USA. [3]Berkeley Geochronology Center, 2455 Ridge Road, Berkeley, CA 94709, USA. [4]Department of Earth and Planetary Sciences, Rutgers University, 610 Taylor Road, Piscataway, NJ 08854, USA.
*Corresponding author. Email: sonia.tikoo@rutgers.edu

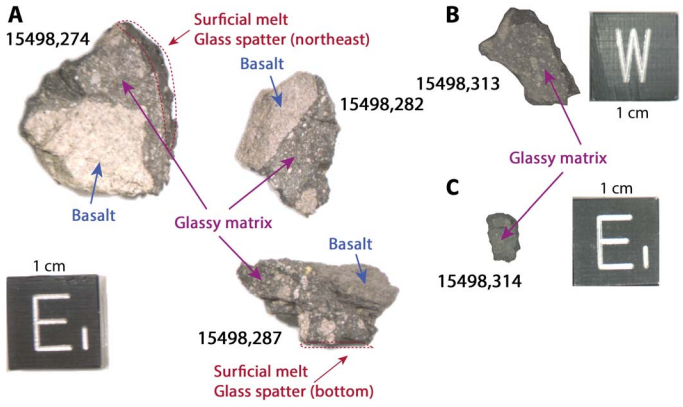

Fig. 1. Mutually oriented 15498 parent chips. (**A**) Chips 15498,274, 15498,282, and 15498,287. (**B**) Chip 15498,313. (**C**) Chip 15498,314. The sample contains abundant mare basalt fragments (blue arrows and labels) within a glassy matrix (purple arrows and labels). Surficial melt glass spatter locations are denoted with red arrows and outlines. The scale cubes have widths of 1 cm. The subsamples and scale cube are oriented following the Johnson Space Center (JSC) system for 15498.

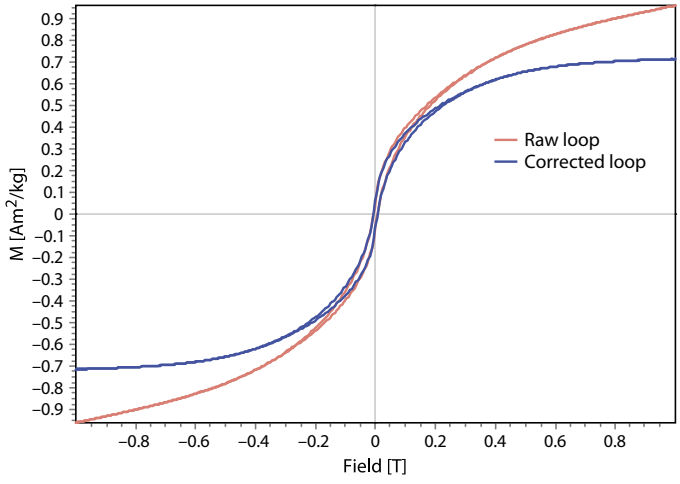

Fig. 2. Hysteresis curves for 15498. The red curve shows the measured data. The blue curve shows the data after application of a paramagnetic slope correction.

Conductive cooling calculations indicate that the glass matrix cooled from above the Curie temperature of kamacite (780°C) to ambient lunar surface temperatures (<100°C) over a period of at least a few hours (see section S1). However, this cooling time scale is long relative to the expected <1-s duration of impact fields when the rock formed. Therefore, impact fields are extremely unlikely to be the source of any TRM or TCRM acquired by the breccia's glass matrix during primary cooling.

Hysteresis data (see section S4) (*39*) and our electron microscopy imaging indicate that, in stark contrast to the multidomain grain size of metal in virtually all lunar crystalline rocks, metal within the glass matrix of 15498 is a mixture of predominantly superparamagnetic to pseudosingle domain grains, with only a relatively small contribution from multidomain grains in lithic fragments (Fig. 2). The presence of these fine-grained magnetic carriers indicates that the melt glass portion of 15498 should provide unusually high-fidelity paleomagnetic records. The relatively low Ni content of kamacite and martensite grains present within the rock suggests that the rock should retain any primary TRM and TCRM through laboratory thermal demagnetization experiments up to maximum temperatures between ~600° and 780°C [which correspond to the austenite-start solid-state phase transformation temperature for the observed martensite compositions and the kamacite Curie temperature, respectively (see section S1)]. In combination, these rock magnetic properties indicate that 15498 is an excellent target for lunar paleomagnetic studies.

A previous analysis of 15498 found that the glass matrix of the sample contained a stable natural remanent magnetization (NRM) component that persisted during alternating field (AF) demagnetization to at least 40 mT and during thermal demagnetization to at least 650°C (*39*, *40*). A paleointensity value of ~2.1 μT was obtained from one subsample (*40*) using a modified Thellier-Thellier (*41*) technique. However, this study was not able to conclusively demonstrate a robust record of the lunar dynamo due to lack of measurements of mutually oriented subsamples, checks for sample alteration during the paleointensity experiment, a detailed characterization of its postformational shock and metamorphic history, and, most importantly, a radiometric age.

RESULTS

Thermochronometry and sample age constraints

The glass matrix of 15498 should have acquired its original NRM during primary cooling. To establish the timing of this event and constrain the possibility of postformational thermal remagnetization, we conducted $^{40}Ar/^{39}Ar$ and $^{38}Ar/^{37}Ar$ thermochronometry on a whole-rock aliquot taken from the interior of a ~1-cm-diameter basalt clast from the interior of sample 15498. We obtained a minimum $^{40}Ar/^{39}Ar$ clast crystallization age of 3310 ± 24 Ma [1 SD analytical uncertainty not including uncertainties in the age of the fluence monitor and decay constant (*42*)]. This value is consistent with the crystallization ages of other studied Apollo 15 mare basalts (*43*, *44*) and is therefore likely close to the true clast crystallization age. Subsequent heating experienced by this clast due to breccia formation and daytime heating on the lunar surface triggered thermally activated diffusive loss of radiogenic ^{40}Ar. The apparent spatial distributions of radiogenic ^{40}Ar ($^{40}Ar^{*}$) and cosmogenic ^{38}Ar ($^{38}Ar_{cos}$) within clast K–rich mesostasis glass and feldspathic glass are consistent with a three-stage thermal history involving (i) clast formation at ~3.3 Ga, (ii) diffusive loss of Ar due to impact heating to peak temperatures of ~500° to ~650°C at the time of breccia lithification (occurring between ~2.5 and 1.0 Ga), and (iii) further Ar loss from daytime heating after the rock was exposed near the lunar surface at ~600 Ma [as indicated by our cosmogenic exposure age measurements (see section S5)] (Fig. 3).

Our inferred lithification age of ~2.5 to 1.0 Ga (with 1.0 Ga being our best estimate) is broadly consistent with other semiquantitative age estimates (~0.9 to 1.8 Ga) obtained from measuring trapped $^{40}Ar/^{36}Ar$ within the melt glass matrix (see section S5) (*45*). The trapped $^{40}Ar/^{36}Ar$ method aims to obtain breccia lithification model ages by measuring the ratio of lunar atmospheric ^{40}Ar to solar wind ^{36}Ar for the implanted component of Ar in the regolith. However, this method is subject to limitations associated with its primary assumptions. First, the trapped ^{40}Ar measured using this technique must have experienced a complex history of (i) formation from decay of ^{40}K in the Moon, (ii) degassing into the exosphere, and (iii) ionization and reimplantation into the lunar regolith, and assumptions are required about the efficiency of each of these processes. The method also assumes that solar wind ^{36}Ar at the Moon is constant with geological time, whereas this quantity

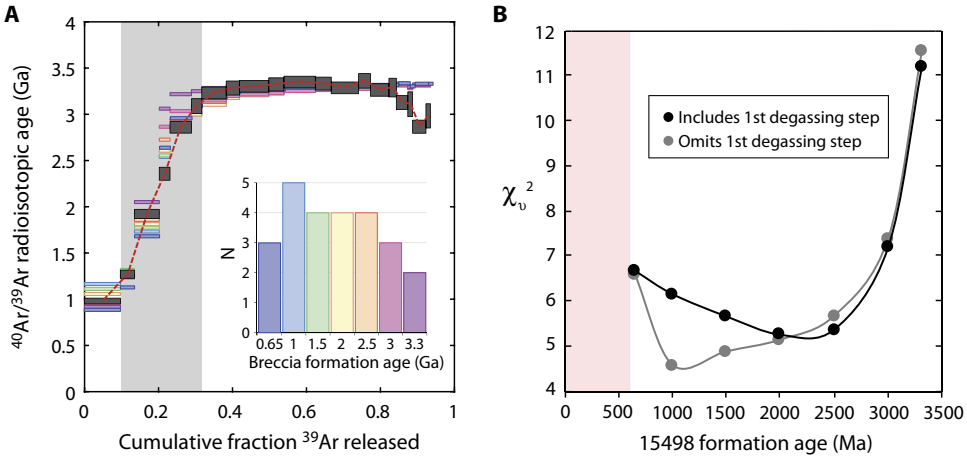

Fig. 3. ^{40}Ar/^{39}Ar thermochronometry constraints on the formation age of breccia 15498. (**A**) Multi-phase, multi-domain diffusion (MP-MDD) model predictions for diffusion of radiogenic ^{40}Ar* experienced by a 1-cm-diameter basalt clast within 15498 resulting from breccia formation between 650 and 3300 Ma (that is, from heating to temperatures ranging between 450° and 675°C), followed by daytime heating to effective mean temperatures ranging between 25° and 56°C after 600 Ma. Observed step heating ages ±1 SD (dark gray boxes) are plotted against the cumulative release fraction of ^{39}Ar released. The 3310 ± 24–Ma age inferred from the HT release steps represents the minimum crystallization age of the basalt clast. The colored steps are model release spectra calculated using MP-MDD model parameters corresponding to breccia formation at varying times (different formation ages are indicated with different colors). The inset displays the number of model degassing steps that are within error of the sample degassing path (individual steps connected by dashed red line) in the LT release fraction (heating steps 2 to 6) for different breccia formation ages (a value of $n = 5$ indicates all steps fit within error of the model). (**B**) Reduced χ^2 misfit values for model release spectra shown in (A). Misfits are shown both including (black circles) and excluding (gray circles) the first degassing step of the heating experiments. Red shaded box indicates formation ages precluded by the cosmogenic exposure age (≤600 Ma).

will actually vary depending on the strength of the lunar magnetic field (that is, its solar wind–shielding capacity) over time. Hence, this method relies on a calibration that accounts for these various factors (each subject to its own uncertainties) to relate the trapped ^{40}Ar/^{36}Ar to a lithification age in geologic time [see the studies of Fagan *et al.* (*45*) and Joy *et al.* (*46*) for further details regarding this method]. The aforementioned uncertainties in the trapped ^{40}Ar/^{36}Ar method encourage the use of an alternative chronometer to obtain complementary sample age constraints, and we were able to do so via our ^{40}Ar/^{39}Ar thermochronology modeling. In any case, we conclude that the breccia most likely formed between 1.0 and 2.5 Ga.

Paleomagnetism

To characterize the NRM in 15498, we studied 20 mutually oriented subsamples of 15498 collected from the glass matrix portions of five mutually oriented parent chips (15498,274, 15498,282, 15498,287, 15498,313, and 15498,314). Twelve subsamples were collected from the interior of 15498, and 8 subsamples were collected from near the edge of the rock (from a distance ≤~3 times the width of the young glass rind coating the sample in the vicinity of each subsample). The proximity of these peripheral subsamples to the young impact melt glass rind enables using thermal demagnetization to conduct a paleomagnetic baked contact test to determine whether the NRM of the interior subsamples predates sampling by the Apollo astronauts (*47*).

Of the 20 total subsamples, 7 subsamples were subjected to stepwise AF demagnetization (Fig. 4A). The remaining 13 subsamples were stepwise thermally demagnetized (Fig. 4B). Among the interior subsamples, we observed a low-coercivity (LC) and low-temperature (LT) magnetization component in all 12 subsamples that typically unblocked below AF levels of ≤6.5 mT and temperatures of ≤125°C, respectively. We observed a medium-coercivity (MC) and medium-temperature (MT) component in most subsamples that typically unblocked between the end of the LC/LT component and ~50 mT/~200°C (see section S2). The LC/LT and MC/MT components are largely non-unidirectional among mutually oriented subsamples (Fig. 5). The relatively low coercivities and unblocking temperatures associated with the LC/LT and MC/MT components suggest that these magnetizations likely represent viscous remanent magnetization (VRM) contamination from the terrestrial field acquired during storage and multiple stages of subdivision and handling at JSC over ≥42 years (see sections S2 and S4).

We also identified a high-coercivity (HC) and high-temperature (HT) component in all 12 interior subsamples that was blocked up to AF levels of at least 290 to 420 mT and temperatures of up to 660° to 750°C (see section S2). The HC/HT component decays linearly toward the origin (Fig. 4), suggesting that it is the characteristic magnetization component. Although there is modest dispersion (up to ~30°) in directions from individual subsamples (Fig. 6), the HC/HT components all generally cluster in the northeastern quadrant of the upper hemisphere. A Watson (*48*, *49*) statistical test for dispersion on a sphere demonstrates that the HC/HT component directions are nonrandom to 99% confidence [that is, the length of the resultant vector of our HC/HT component directions ($R = 11.5$) was greater than the critical value ($R_o = 6.55$ for 12 subsamples)] and therefore likely have a common origin. The low ratio of NRM to isothermal remanent magnetization (IRM) (≪0.1) suggests that this component was not imparted by a strong-field IRM (see section S3). The HC magnetization is unlikely to be a shock remanent magnetization (SRM), given that SRM acquired at pressures of <3 GPa is typically acquired by low-coercivity grains (see section S4) (*50*, *51*). Because single-domain kamacite grains (which dominantly carry the remanence in 15498) should not retain a terrestrial VRM after laboratory heating to temperatures above ~125°C (*52*), the persistence of the HT component to temperatures ≥660°C precludes its origin as a VRM. Crystallization remanent magnetization (CRM) is also excluded because the metal grains are in the form of primary low-Ni kamacite and martensite (and have not recrystallized to plessite or to Widmanstätten taenite and kamacite).

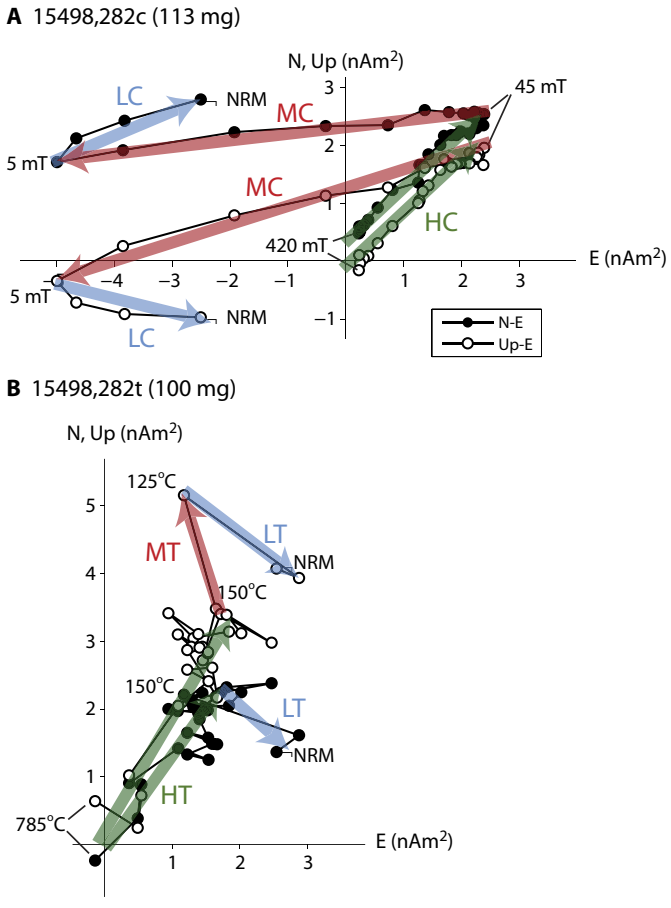

Fig. 4. Vector endpoint diagrams showing demagnetization of 15498 subsamples. (**A**) AF demagnetization of subsample 282c. (**B**) Thermal demagnetization of subsample 282t. Open and closed circles represent projections of the NRM vector onto the vertical (Up-E) and horizontal planes (N-E), respectively. Blue, red, and green arrows denote LC/LT, MC/MT, and HC/HT components, respectively. Subsample masses as well as selected AF levels and temperature steps are labeled.

We obtained high-quality Thellier-Thellier paleointensity values of 5 ± 2 μT (mean ± 1σ) from the HT components of six of the interior subsamples (Fig. 7). These values are broadly consistent with our anhysteretic remanent magnetization (ARM) and IRM paleointensity measurements on the HC components of four AF-demagnetized subsamples, which yielded values ranging between ~600 nT and ~2 μT [within the factor 2 to 5 uncertainties on the latter values (*6*)]. It is conceivable that the remanence being carried is not purely TRM and that some martensite may have acquired TCRM upon formation. However, if the NRM of 15498 is a TCRM, the paleointensities inferred from our Thellier experiments would likely represent lower limits due to the inefficiency of CRM relative to TRM (*53*). Regardless, paleointensities derived from TCRM are usually within several tens of percent of the actual value (*54*). Therefore, we suspect that our paleointensity results are reasonably accurate even if the remanence is not a pure TRM.

In contrast, four of the five thermally demagnetized peripheral subsamples taken from near the young melt glass rind were fully demagnetized by 360°C, and two of the three AF-demagnetized peripheral subsamples were fully demagnetized by ac fields of 20 mT. The only subsample that contained a magnetization component with the same direction as the HC/HT component observed within the interior subsamples was the subsample collected the farthest away (0.7 cm) from the melt glass rind (274v3). Furthermore, the inferred NRM intensities of these subsamples are, on average, ~90% lower than those of the interior subsamples (see Fig. 8 and section S2). The general absence of HC and HT magnetization within peripheral subsamples suggests that they were thermally demagnetized on the Moon when the impact melt glass was emplaced on the surface of the rock. Collectively, these data are consistent with a positive baked contact test for 15498 and indicate that the HC/HT component observed in the interior subsamples is very likely a TRM acquired during primary cooling in the presence of a temporally stable ambient field on the Moon.

DISCUSSION

The ~5-μT paleointensities obtained from the melt glass matrix of 15498 are ~1000 times stronger than the field measured by astronauts

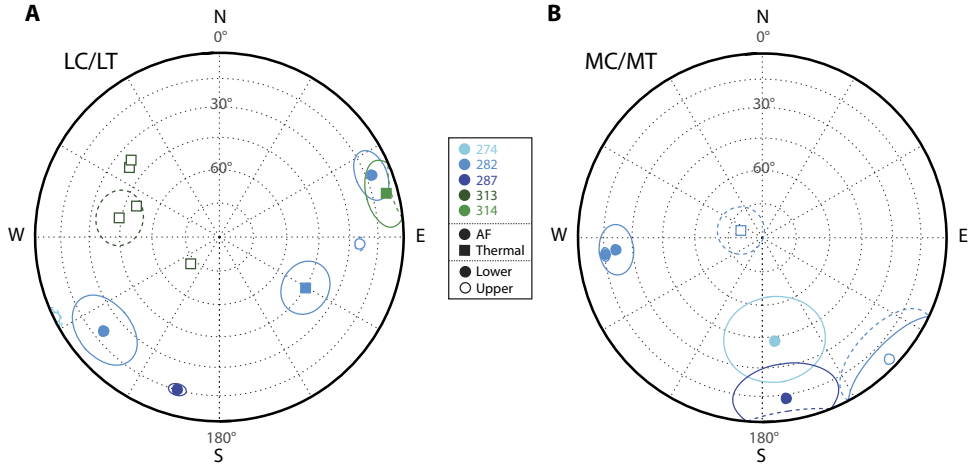

Fig. 5. Equal-area stereographic projections of LC/LT and MC/MT magnetization components observed for interior subsamples of 15498. (**A**) LC (circles) and LT (squares) component directions. (**B**) MC (circles) and MT (squares) component directions. Lines encircling component directions represent the maximum angular deviations associated with each direction. Open symbols (dashed lines) represent directions in the upper hemisphere, whereas filled symbols (solid lines) represent directions in the lower hemisphere. Subsamples from parent chips 274, 282, 287, 313, and 314 are denoted with light blue, medium blue, dark blue, dark green, and light green symbols, respectively.

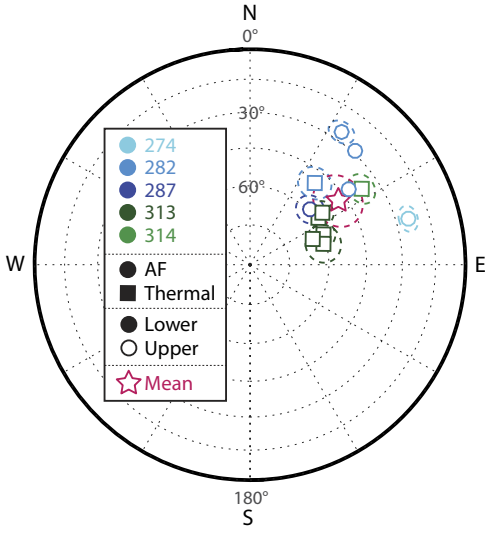

Fig. 6. Equal-area stereographic projection of HC and HT magnetization component directions. Shown directions are observed for mutually oriented matrix glass subsamples from the interior of 15498. Symbols and surrounding ellipses represent directions and associated maximum angular deviation values obtained from principal component analysis. AF and thermally demagnetized subsamples are displayed using circles and squares, respectively. Subsamples from parent chips 274, 282, 287, 313, and 314 are shown by light blue, medium blue, dark blue, dark green, and light green symbols, respectively. Open symbols (dashed lines) represent directions in the upper hemisphere, and filled symbols (solid lines) represent directions in the lower hemisphere. The Fisher mean direction and α_{95} confidence interval (star and surrounding ellipse, respectively) are shown.

at the Apollo 15 site (*55*), ~10 times stronger than the largest remanent crustal fields measured at any lunar landing site (Apollo 16), and several orders of magnitude greater than external field sources like the Earth, Sun, and galactic magnetic fields (*55*). The most likely mechanisms capable of generating ~5-μT fields at the lunar surface at 1 to 2.5 Ga are impact fields and a core dynamo. Because the slow primary cooling time scale of 15498 excludes an impact field origin for the observed TRM, our data strongly indicate that the glass matrix portion of 15498 preserves a dynamo record.

Our data indicate that the lunar core dynamo persisted until at least ~1.0 to ~2.5 Ga, thereby extending the known lifetime of the dynamo by ~1.0 billion to ~2.5 billion years [from the previous youngest dynamo record observed in 3.56-Ga mare basalts (*5*)]. Exactly when the lunar dynamo ceased remains unclear. Given the expected geophysical properties of the lunar interior, no current dynamo scenarios powered by large impacts or purely thermal convection predict that the magnetic field could persist this late in lunar history. Thermal evolution models suggest that thermochemical convection produced by core crystallization could generate a ~1-μT dynamo field that persisted (either continuously or in an intermittent "start-stop" regime) beyond ~1.6 Ga (*24*, *26*). However, according to current scaling laws for convective dynamos, thermochemical convection alone may not be able to reproduce the high ~20- to ~110-μT surface fields inferred for Apollo samples aged 4.25 to 3.56 Ga (*6*). In contrast, a precession dynamo may be capable of generating ~10- to ~100-μT fields for the period before 3.56 Ga (*15*, *16*), but persistence of such a dynamo beyond ~2 Ga would likely require that the Moon's orbit receded from the Earth at a rate far slower than expected (*6*, *8*). Given these constraints, no single dynamo generation mechanism proposed thus far can readily reproduce the paleointensity record inferred from Apollo samples. One possible solution is that the dynamo may have been powered by at least two distinct mechanisms operating during early and late lunar history. A second possible solution

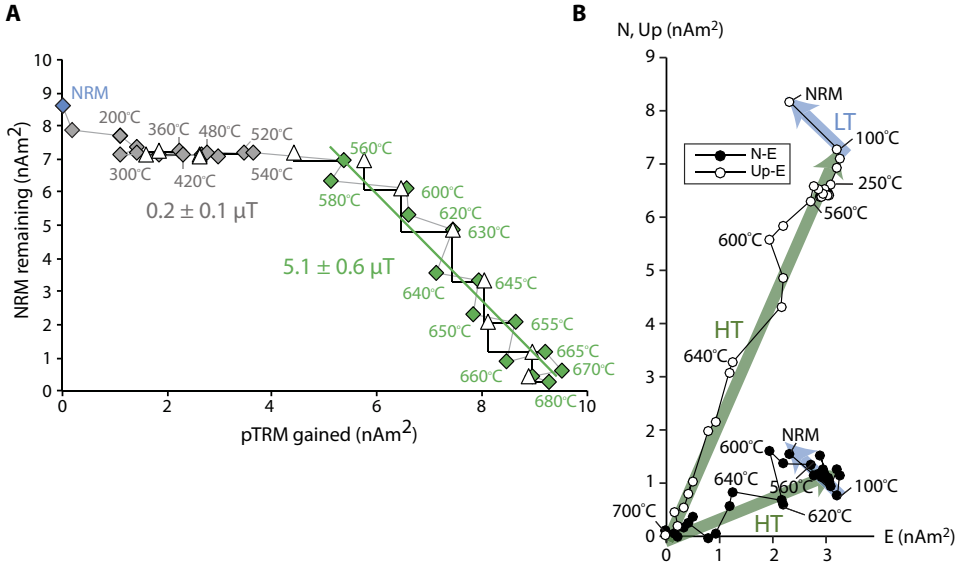

Fig. 7. Thellier-Thellier paleointensity experiment for subsample 15498,313e. (**A**) Arai plot displaying NRM lost during progressive thermal demagnetization (ordinate) versus laboratory pTRM gained (abscissa). Peak temperatures for selected steps are shown. pTRM checks for alteration are shown as triangles. Paleointensities for unblocking temperature ranges of 250° to 540°C and 560° to 680°C are denoted with dark gray and green symbols, respectively. Gray segments link consecutive thermal steps. (**B**) Vector endpoint diagram showing zero-field thermal demagnetization steps for subsample 313e. LT and HT components are denoted using blue and green symbols, respectively. Paleointensity experiments were conducted following the IZZI protocol (alternating zero-field and in-field measurements).

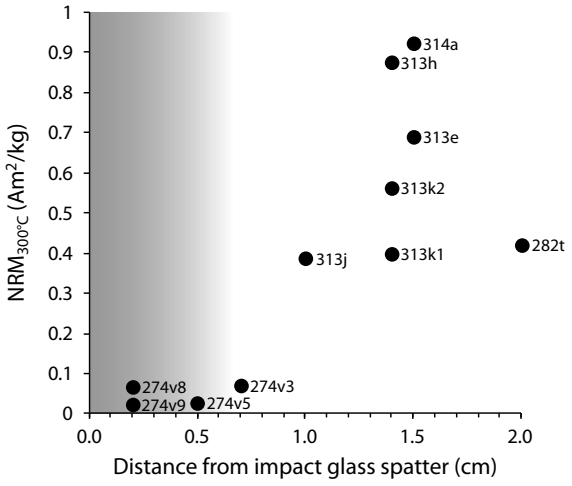

Fig. 8. Magnetization versus distance from the peripheral impact glass spatter. Shown are residual magnetization values for thermally demagnetized 15498 matrix glass subsamples after heating to 300°C. Individual subsample names are labeled. The gray shaded box denotes the zone likely to have been remagnetized by emplacement of the impact glass spatter (approximately three half-widths of the local glass spatter thickness).

is that dynamo was powered by a single bistable mechanism that transitioned from a strong-dipole dominated state to a weaker multipolar state after 3.56 Ga (*56*).

METHODS

Paleomagnetic and rock magnetic analyses

All paleomagnetic measurements were conducted using a 2G Enterprises Superconducting Rock Magnetometer 755 located within a magnetically shielded room (ambient field of <200 nT) in the Massachusetts Institute of Technology (MIT) Paleomagnetism Laboratory. The magnetometer is equipped with automated AF demagnetization, sample handling, and rock magnetic remanence characterization capabilities (*57*). Purely nondestructive static three-axis AF demagnetization experiments were conducted on 7 of the 20 total subsamples up to peak ac fields of at least 290 mT. Purely thermal demagnetization was conducted on nine subsamples up to maximum temperatures of 660° to 700°C, or until samples were fully demagnetized, in a new controlled oxygen fugacity oven (*58*). Thermal experiments were conducted in an H_2-CO_2 atmosphere at 1 log unit below the iron-wüstite buffer. The four remaining subsamples were AF-pretreated up to peak ac fields of 35 mT and then thermally demagnetized. The subsamples were measured in differing orientations, and the demagnetization data were subsequently rotated into a mutually oriented reference frame for analysis. Principal component analysis was used to determine the best-fit directions for all observed magnetization components (*59*). Thellier-Thellier paleointensity experiments were conducted on six of the thermal demagnetization subsamples following the IZZI (in-field, zero-field, zero-field, in-field) protocol (*60*), including partial TRM (pTRM) checks for alteration. ARM and/or IRM paleointensities (*2*, *5*, *61*) were determined for four subsamples. Full details of the demagnetization and paleointensity experiments are provided in section S3. Remanence-based rock magnetic experiments (for example, ARM and IRM acquisition and demagnetization) were conducted at MIT. Hysteresis and first-order reversal curve (FORC) measurements were conducted using a vibrating sample magnetometer at the Institute for Rock Magnetism at the University of Minnesota (see section S4).

$^{40}Ar/^{39}Ar$ and $^{38}Ar/^{37}Ar$ thermochronology

All $^{40}Ar/^{39}Ar$ and $^{38}Ar/^{37}Ar$ thermochronometry experiments were conducted at the Berkeley Geochronology Center. Using the procedures described in previous works (*4*, *5*, *62*), we conducted stepwise degassing $^{40}Ar/^{39}Ar$ and $^{38}Ar/^{37}Ar$ experiments on one (~2 mg) whole-rock aliquot of a basalt clast (referred to as 282-1 herein) located adjacent to the glass matrix portion of parent chip 15498,282 that we used for paleomagnetic analyses. Additional stepwise degassing experiments conducted on two whole-rock aliquots of matrix glass yielded complex, discordant age spectra from which no plateau age could be inferred due to the presence of excess nonradiogenic (trapped) ^{40}Ar and solar wind ^{36}Ar. This degassing behavior has been observed for many other lunar impact glasses and regoliths (*63*). Because it was not possible to directly obtain ages for the matrix glass samples, we do not discuss these experiments further. Apparent $^{40}Ar/^{39}Ar$ ages for each degassing step were calculated relative to the Hb3gr fluence monitor [age, 1081 Ma (*42*)] using the decay constants of Renne *et al.* (*42*) and the isotopic abundances of Steiger and Jäger (*64*). We also determined apparent cosmogenic ^{38}Ar exposure ages for each degassing step following procedures described in previous works (*4*, *5*, *65*). Following Shea *et al.* (*4*), we constructed multi-phase, multi-diffusion domain (MP-MDD) model fits to the $^{40}Ar/^{39}Ar$ age spectrum and the cosmogenic ^{38}Ar age spectrum to quantify the diffusion of radiogenic ^{40}Ar ($^{40}Ar^*$) and cosmogenic ^{38}Ar ($^{38}Ar_{cos}$) in our sample in the context of various possible thermal histories. All modeled thermal histories include (i) the initial formation of the basalt clast, (ii) diffusive loss of Ar due to impact heating at the time of breccia lithification, and (iii) further loss of Ar from daytime heating while the rock was exposed near the lunar surface before its collection. Full details regarding our MP-MDD models are given in section S5.

SUPPLEMENTARY MATERIALS

Supplementary material for this article is available at http://advances.sciencemag.org/cgi/content/full/3/8/e1700207/DC1

section S1. Sample 15498
section S2. NRM behavior
section S3. Paleointensity
section S4. Rock magnetic properties
section S5. $^{40}Ar/^{39}Ar$ and $^{38}Ar/^{37}Ar$ thermochronology
fig. S1. Apollo 15 landing site and 15498 sampling context.
fig. S2. Sample 15498.
fig. S3. Backscattered scanning electron microscopy images of 15498 matrix showing absence of post-lithification microfracturing.
fig. S4. BSEM images of FeNi grains in 15498.
fig. S5. Equal-area stereographic projections of LC/LT and MC/MT magnetization components observed for peripheral subsamples of 15498.
fig. S6. AF demagnetization of sample 15498,282a over the range of the HC component.
fig. S7. Thellier-Thellier paleointensity experiments for subsamples 15498,313k1 and 15498,313k2 following the IZZI variant.
fig. S8. Paleointensity fidelity limit tests for 15498.
fig. S9. FORC distribution for sample 15498,287b1.
fig. S10. Rock magnetic experiments on 15498,282a.
fig. S11. PRM acquisition by 15498 subsample 15498,282a.
fig. S12. VRM decay experiment on sample 15498,282c.
fig. S13. The predicted effects of 600 Ma of solar heating at the lunar surface, calculated using the 15498 MP-MDD model.
fig. S14. Arrhenius plots with calculated diffusion coefficients for ^{39}Ar and ^{37}Ar released during the first 20 release steps.
fig. S15. Schematic depicting time-temperature conditions underlying our thermochronological models.
fig. S16. 15498 MP-MDD model predictions for diffusion of $^{40}Ar^*$ resulting from impact heating at 2000 Ma (to temperatures ranging between 450° and 675°C), followed by daytime heating to an effective mean temperature of 69°C after 600 Ma.

fig. S17. 15498 MP-MDD model predictions for diffusion of $^{40}Ar^*$ resulting from impact heating at various times in lunar history (to temperatures ranging between 450° and 675°C), followed by daytime heating to effective mean temperatures ranging between 35° and 56°C after 600 Ma.
fig. S18. 15498 MP-MDD model age spectra incorporating diffusion of $^{40}Ar^*$ resulting from impact heating at 650 Ma (to temperatures ranging between 450° and 675°C), followed by daytime heating to an effective mean temperature of 25°C after 600 Ma.
table S1. WDS measurements of metal grains in 15498 thin sections 298 and 299.
table S2A. NRM components identified for interior matrix glass subsamples of 15498.
table S2B. NRM components identified for peripheral matrix glass subsamples of 15498.
table S2C. Fisher mean component directions derived from 15498 data in table S2A.
table S3A. Thellier-Thellier paleointensity determinations for 15498 subsamples.
table S3B. Comparison of pTRM and pTRM check values for 15498 subsamples.
table S3C. ARM paleointensity determinations for 15498 subsamples.
table S3D. IRM paleointensity determinations for 15498 subsamples.
table S4. Rock magnetic and hysteresis parameters.
table S5. Anisotropy of ARM (85-mT ac field with 0.01-mT dc field).
table S6. Complete $^{40}Ar/^{39}Ar$ incremental heating results.
table S7. Oxide weight percent compositions of K-bearing phases in basalt clast 15498-282-1.
table S8. Summary of MP-MDD model parameters with cosmogenic ^{38}Ar production rates for 15498.
table S9. Summary of $^{40}Ar/^{39}Ar$ chronology for 15498.
table S10. Reduced χ^2 misfit statistics for best-fit thermochronometry models for a variety of breccia formation ages.
data file S1. 15498 demagnetization data sets.
data file S2. 15498 Thellier-Thellier paleointensity data sets.
References (*66*–*125*)

REFERENCES AND NOTES

1. C. Cournède, J. Gattacceca, P. Rochette, Magnetic study of large Apollo samples: Possible evidence for an ancient centered dipolar field on the Moon. *Earth Planet. Sci. Lett.* **331–332**, 31–42 (2012).
2. I. Garrick-Bethell, B. P. Weiss, D. L. Shuster, J. Buz, Early lunar magnetism. *Science* **323**, 356–359 (2009).
3. L. L. Hood, Central magnetic anomalies of Nectarian-aged lunar impact basins: Probable evidence for an early core dynamo. *Icarus* **211**, 1109–1128 (2011).
4. E. K. Shea, B. P. Weiss, W. S. Cassata, D. L. Shuster, S. M. Tikoo, J. Gattacceca, T. L. Grove, M. D. Fuller, A long-lived lunar core dynamo. *Science* **335**, 453–456 (2012).
5. C. Suavet, B. P. Weiss, W. S. Cassata, D. L. Shuster, J. Gattacceca, L. Chan, I. Garrick-Bethell, J. W. Head, T. L. Grove, M. D. Fuller, Persistence and origin of the lunar core dynamo. *Proc. Natl. Acad. Sci. U.S.A.* **110**, 8453–8458 (2013).
6. B. P. Weiss, S. M. Tikoo, The lunar dynamo. *Science* **346**, 1246753 (2014).
7. K. Lawrence, C. Johnson, L. Tauxe, J. Gee, Lunar paleointensity measurements: Implications for lunar magnetic evolution. *Phys. Earth Planet. Inter.* **168**, 71–87 (2008).
8. S. M. Tikoo, B. P. Weiss, W. S. Cassata, D. L. Shuster, J. Gattacceca, E. A. Lima, C. Suavet, F. Nimmo, M. D. Fuller, Decline of the lunar core dynamo. *Earth Planet. Sci. Lett.* **404**, 89–97 (2014).
9. M. Fuller, Lunar magnetism—A retrospective view of the Apollo sample magnetic studies. *Phys. Chem. Earth* **23**, 725–735 (1998).
10. A. J. Evans, M. T. Zuber, B. P. Weiss, S. M. Tikoo, A wet, heterogeneous lunar interior: Lower mantle and core dynamo evolution. *J. Geophys. Res.* **119**, 1061–1077 (2014).
11. W. Konrad, T. Spohn, Thermal history of the Moon: Implications for an early core dynamo and post-accertional magmatism. *Adv. Space Res.* **19**, 1511–1521 (1997).
12. M. Laneuville, M. A. Wieczorek, D. Breuer, N. Tosi, Asymmetric thermal evolution of the Moon. *J. Geophys. Res.* **118**, 1435–1452 (2013).
13. D. R. Stegman, A. M. Jellinek, S. A. Zatman, J. R. Baumgardner, M. A. Richards, An early lunar core dynamo driven by thermochemical mantle convection. *Nature* **421**, 143–146 (2003).
14. M. Le Bars, M. A. Wieczorek, Ö. Karatekin, D. Cébron, M. Laneuville, An impact-driven dynamo for the early Moon. *Nature* **479**, 215–218 (2011).
15. C. A. Dwyer, D. J. Stevenson, F. Nimmo, A long-lived lunar dynamo driven by continuous mechanical stirring. *Nature* **479**, 212–214 (2011).
16. S. Stanley, B. Y. Tian, B. P. Weiss, S. M. Tikoo, The ancient lunar dynamo: How to resolve the intensity and duration conundrums. *Proc. Lunar Planet. Sci. Conf.* **48**, 1462 (2017).
17. R. C. Weber, P.-Y. Lin, E. J. Garnero, Q. Williams, P. Lognonne, Seismic detection of the lunar core. *Science* **331**, 309–312 (2011).
18. J. G. Williams, A. S. Konopliv, D. H. Boggs, R. S. Park, D.-N. Yuan, F. G. Lemoine, S. Goossens, E. Mazarico, F. Nimmo, R. C. Weber, S. W. Asmar, H. J. Melosh, G. A. Neumann, R. J. Phillips, D. E. Smith, S. C. Solomon, M. M. Watkins, M. A. Wieczorek, J. C. Andrews-Hanna, J. W. Head, W. S. Kiefer, I. Matsuyama, P. J. McGovern, G. J. Taylor, M. T. Zuber, Lunar interior properties from the GRAIL mission. *J. Geophys. Res.* **119**, 1546–1578 (2014).
19. R. F. Garcia, J. Gagnepain-Beyneix, S. Chevrot, P. Lognonné, Very preliminary reference Moon model. *Phys. Earth Planet. Inter.* **188**, 96–113 (2011).
20. L. L. Hood, D. L. Mitchell, R. P. Lin, M. H. Acuna, A. B. Binder, Initial measurements of the lunar induced magnetic dipole moment using Lunar Prospector Magnetometer data. *Geophys. Res. Lett.* **26**, 2327–2330 (1999).
21. Z. Jing, Y. Wang, Y. Kono, T. Yu, T. Sakamaki, C. Park, M. L. Rivers, S. R. Sutton, G. Shen, Sound velocity of Fe–S liquids at high pressure: Implications for the Moon's molten outer core. *Earth Planet. Sci. Lett.* **396**, 78–87 (2014).
22. A. S. Konopliv, A. B. Binder, L. L. Hood, A. B. Kucinskas, W. L. Sjogren, J. G. Williams, Improved gravity field of the moon from lunar prospector. *Science* **281**, 1476–1480 (1998).
23. H. Shimizu, F. Matsushima, F. Takahashi, H. Shibuya, H. Tsunakawa, Constraint on the lunar core size from electromagnetic sounding based on magnetic field observations by an orbiting satellite. *Icarus* **222**, 32–43 (2013).
24. M. Laneuville, M. A. Wieczorek, D. Breuer, J. Aubert, G. Morard, T. Rückriemen, A long-lived lunar dynamo powered by core crystallization. *Earth Planet. Sci. Lett.* **401**, 251–260 (2014).
25. N. Zhang, E. M. Parmentier, Y. Liang, A 3-D numerical study of the thermal evolution of the Moon after cumulate mantle overturn: The importance of rheology and core solidification. *J. Geophys. Res.* **118**, 1789–1804 (2013).
26. A. Scheinberg, K. M. Soderlund, G. Schubert, Magnetic field generation in the lunar core: The role of inner core growth. *Icarus* **254**, 62–71 (2015).
27. S. M. Tikoo, B. P. Weiss, J. Buz, E. A. Lima, E. K. Shea, G. Melo, T. L. Grove, Magnetic fidelity of lunar samples and implications for an ancient core dynamo. *Earth Planet. Sci. Lett.* **337–338**, 93–103 (2012).
28. M. A. Wieczorek, B. L. Jolliff, A. Khan, M. E. Pritchard, B. P. Weiss, J. G. Williams, L. L. Hood, K. Righter, C. R. Neal, C. K. Shearer, I. S. McCallum, S. Tompkins, B. R. Hawke, C. Peterson, J. J. Gillis, B. Bussey, The constitution and structure of the lunar interior. *Rev. Mineral. Geochem.* **60**, 221–364 (2006).
29. J. Buz, B. P. Weiss, S. M. Tikoo, D. L. Shuster, J. Gattacceca, T. L. Grove, Magnetism of a very young lunar glass. *J. Geophys. Res.* **120**, 1720–1735 (2015).
30. L. L. Hood, N. A. Artemieva, Antipodal effects of lunar basin-forming impacts: Initial 3D simulations and comparisons with observations. *Icarus* **193**, 485–502 (2008).
31. D. A. Crawford, P. H. Schultz, Electromagnetic properties of impact-generated plasma, vapor and debris. *Int. J. Impact Eng.* **23**, 169–180 (1999).
32. L. J. Srnka, Spontaneous magnetic field generation in hypervelocity impacts. *Proc. Lunar Planet. Sci. Conf.* **8**, 785–792 (1977).
33. B. Mason, Mineralogy and petrology of polymict breccia 15498, in *The Apollo 15 Lunar Samples* (The Lunar Science Institute, 1972), pp. 137–139.
34. G. Ryder, Ed., *Catalog of Apollo 15 Rocks* (NASA Curatorial Branch, 1985), vol. 72.
35. S. K. Vetter, J. W. Shervais, M. M. Lindstrom, Petrology and geochemistry of olivine-normative and quartz-normative basalts from regolith breccia 15498: New diversity in Apollo 15 mare basalts. *Proc. Lunar Planet. Sci. Conf.* **18**, 255–271 (1988).
36. P. Lambert, Fractures induced by shock in quartz and feldspar. *Mineral. Mag.* **43**, 527–533 (1979).
37. D. R. Uhlmann, L. C. Klein, Crystallization kinetics, viscous flow and thermal histories of lunar breccias 15286 and 15498. *Proc. Lunar Planet. Sci. Conf.* **7**, 2529–2541 (1976).
38. G. W. Pearce, G. S. Hoye, D. W. Strangway, B. M. Walker, L. A. Taylor, Some complexities in the determination of lunar paleointensities. *Proc. Lunar Planet. Sci. Conf.* **7**, 3271–3297 (1976).
39. W. A. Gose, G. W. Pearce, D. W. Strangway, J. Carnes, Magnetism of Apollo 15 samples, in *The Apollo 15 Lunar Samples* (The Lunar Science Institute, 1972), pp. 430–434.
40. W. A. Gose, D. W. Strangway, G. W. Pearce, A determination of the intensity of the ancient lunar magnetic field. *The Moon* **7**, 196–201 (1973).
41. E. Thellier, O. Thellier, Sur l'intensité du champ magnétique terrestre dans le passé historique et géologique. *Ann. Geophys.* **15**, 285–376 (1959).
42. P. R. Renne, G. Balco, K. R. Ludwig, R. Mundil, K. Min, Response to the comment by W.H. Schwarz et al. on "Joint determination of ^{40}K decay constants and $^{40}Ar^*/^{40}K$ for the Fish Canyon sanidine standard, and improved accuracy for $^{40}Ar/^{39}Ar$ geochronology" by P.R. Renne et al. (2010). *Geochim. Cosmochim. Acta* **75**, 5097–5100 (2011).
43. D. L. Shuster, W. S. Cassata, Paleotemperatures at the lunar surfaces from open system behavior of cosmogenic ^{38}Ar and radiogenic ^{40}Ar. *Geochim. Cosmochim. Acta* **155**, 154–171 (2015).
44. D. Stöffler, G. Ryder, B. A. Ivanov, N. A. Artemieva, M. J. Cintala, R. A. F. Grieve, Cratering history and lunar chronology. *Rev. Mineral. Geochem.* **60**, 519–596 (2006).
45. A. L. Fagan, K. H. Joy, D. D. Bogard, D. A. Kring, Ages of globally distributed lunar paleoregoliths and soils from 3.9 Ga to the present. *Earth Moon Planets* **112**, 59–71 (2014).
46. K. H. Joy, D. A. Kring, D. D. Bogard, D. S. McKay, M. E. Zolensky, Re-examination of the formation ages of the Apollo16 regolith breccias. *Geochim. Cosmochim. Acta* **75**, 7208–7225 (2011).

47. C. W. F. Everitt, J. A. Clegg, A field test of palaeomagnetic stability. *Geophys. J. Int.* **6**, 312–319 (1962).
48. G. S. Watson, Analysis of dispersion on a sphere. *Geophys. J. Roy. Astron. Soc.* **7**, 153–159 (1956).
49. G. S. Watson, A test for randomness of directions. *Geophys. J. Roy. Astron. Soc.* **7**, 160–161 (1956).
50. J. Gattacceca, M. Boustie, L. Hood, J.-P. Cuq-Lelandais, M. Fuller, N. S. Bezaeva, T. de Resseguier, L. Berthe, Can the lunar crust be magnetized by shock: Experimental groundtruth. *Earth Planet. Sci. Lett.* **299**, 42–53 (2010).
51. S. M. Tikoo, J. Gattacceca, N. L. Swanson-Hysell, B. P. Weiss, C. Suavet, C. Cournède, Preservation and detectability of shock-induced magnetization. *J. Geophys. Res.* **120**, 1461–1475 (2015).
52. I. Garrick-Bethell, B. P. Weiss, Kamacite blocking temperatures and applications to lunar magnetism. *Earth Planet. Sci. Lett.* **294**, 1–7 (2010).
53. D. J. Dunlop, K. S. Argyle, Thermoremanence, anhysteretic remanence and susceptibility of submicron magnetites: Nonlinear field dependence and variation with grain size. *J. Geophys. Res.* **102**, 20199–20210 (1997).
54. K. Fabian, Thermochemical remanence acquisition in single-domain particle ensembles: A case for possible overestimation of the geomagnetic paleointensity. *Geochem. Geophys. Geosyst.* **10**, Q06Z03 (2009).
55. P. Dyal, C. W. Parkin, W. D. Daily, Magnetism and the interior of the moon. *Rev. Geophys. Space Phys.* **12**, 568–591 (1974).
56. T. Gastine, L. Duarte, J. Wicht, Dipolar versus multipolar dynamos: The influence of the background density stratification. *Astron. Astrophys.* **546**, A19 (2012).
57. J. L. Kirschvink, R. E. Kopp, T. D. Raub, C. T. Baumgartner, J. W. Holt, Rapid, precise, and high-sensitivity acquisition of paleomagnetic and rock-magnetic data: Development of a low-noise automatic sample changing system for superconducting rock magnetometers. *Geochem. Geophys. Geosyst.* **9**, Q05Y01 (2008).
58. C. Suavet, B. P. Weiss, T. L. Grove, Controlled-atmosphere thermal demagnetization and paleointensity analyses of extraterrestrial rocks. *Geochem. Geophys. Geosyst.* **15**, 2733–2743 (2014).
59. J. L. Kirschvink, The least-squares line and plane and the analysis of palaeomagnetic data. *Geophys. J. Roy. Astron. Soc.* **62**, 699–718 (1980).
60. L. Tauxe, H. Staudigel, Strength of the geomagnetic field in the Cretaceous Normal Superchron: New data from submarine basaltic glass of the Troodos Ophiolite. *Geochem. Geophys. Geosyst.* **5**, Q02H06 (2004).
61. Y. Yu, Paleointensity determination using anhysteretic remanence and saturation isothermal remanence. *Geochem. Geophys. Geosyst.* **11**, Q02Z12 (2010).
62. W. S. Cassata, P. R. Renne, D. L. Shuster, Argon diffusion in plagioclase and implications for thermochronometry: A case study from the Bushveld Complex, South Africa. *Geochim. Cosmochim. Acta* **73**, 6600–6612 (2009).
63. L. Husain, ^{40}Ar-^{39}Ar chronology and cosmic ray exposure ages of the Apollo 15 samples. *J. Geophys. Res.* **79**, 2588–2606 (1974).
64. R. H. Steiger, E. Jäger, Subcommission on geochronology: Convention on the use of decay constants in geo- and cosmochronology. *Earth Planet. Sci. Lett.* **36**, 359–362 (1977).
65. W. S. Cassata, D. L. Shuster, P. R. Renne, B. P. Weiss, Evidence for shock heating and constraints on Martian surface temperatures revealed by ^{40}Ar/^{39} Ar thermochronometry of Martian meteorites. *Geochim. Cosmochim. Acta* **74**, 6900–6920 (2010).
66. D. R. Scott, A. F. Worden, J. B. Irwin, Crew observations, in *Apollo 15 Preliminary Science Report*, J. P. Allen, Ed. (National Aeronautics and Space Administration, 1972).
67. D. B. J. Bussey, P. D. Spudis, B. R. Hawke, P. G. Lucey, G. J. Taylor, Geology and composition of the Apennine mountains, lunar Imbrium basin. *Proc. Lunar Planet. Sci. Conf.* **29**, 1352 (1998).
68. P. D. Spudis, G. A. Swann, R. Greeley, The formation of Hadley Rille and implications for the geology of the Apollo 15 region. *Proc. Lunar Planet. Sci. Conf.* **18**, 243–254 (1988).
69. B. W. Chappell, D. H. Green, Chemical compositions and petrogenetic relationships in Apollo 15 mare basalts. *Earth Planet. Sci. Lett.* **18**, 237–246 (1973).
70. E. Dowty, M. Prinz, K. Keil, Composition, mineralogy, and petrology of 28 mare basalts from Apollo 15 rake samples. *Proc. Lunar Planet. Sci. Conf.* **4**, 423 (1973).
71. P. A. Helmke, D. P. Blanchard, L. A. Haskin, K. M. Telander, C. K. Weiss, J. W. Jacobs, Major and trace elements in crystaline rocks from Apollo 15. *Proc. Lunar Planet. Sci. Conf.* **4**, 349 (1973).
72. J. M. Rhodes, Major element chemistry of Apollo 15 mare basalts, in *The Apollo 15 Lunar Samples* (The Lunar Science Institute, 1972), pp. 250–252.
73. J. M. Rhodes, N. J. Hubbard, Chemistry, classification, and petrogenesis of Apollo 15 mare basalts. *Proc. Lunar Planet. Sci. Conf.* **4**, 1127–1148 (1973).
74. P. D. Spudis, G. Ryder, Geology and petrology of the Apollo 15 landing site: Past, present, and future understanding. *Eos. Trans. AGU* **66**, 721–726 (1985).
75. A. R. Duncan, M. K. Sher, Y. C. Abraham, A. J. Erlank, J. P. Willis, L. H. Ahrens, Interpretation of the compositional variability of Apollo 15 soils. *Proc. Lunar Planet. Sci. Conf.* **6**, 2309–2320 (1975).
76. G. Ryder, D. Bogard, D. Garrison, Probable age of Autolycus and calibration of lunar stratigraphy . *Geology* **19**, 143–146 (1991).
77. T. S. Culler, T. A. Becker, R. A. Muller, P. R. Renne, Lunar impact history from ^{40}Ar/^{39}Ar dating of glass spherules. *Science* **287**, 1785–1788 (2000).
78. B. R. Hawke, D. T. Blewett, P. G. Lucey, G. A. Smith, J. F. Bell, B. A. Campbell, M. S. Robinson, The origin of lunar crater rays. *Icarus* **170**, 1–16 (2004).
79. C. H. Simonds, Thermal regimes in impact melts and the petrology of the Apollo 17 Station 6 boulder. *Proc. Lunar Planet. Sci. Conf.* **6**, 641–672 (1975).
80. J. Gattacceca, L. Berthe, M. Boustie, F. Vadeboin, P. Rochette, T. De Resseguier, On the efficiency of shock magnetization processes. *Phys. Earth Planet. Inter.* **166**, 1–10 (2008).
81. T. Nagata, Introductory notes on shock remanent magnetization and shock demagnetization of igneous rocks. *Pure Appl. Geophys.* **89**, 159–177 (1971).
82. J. Pohl, U. Bleil, U. Hornemann, Shock magnetization and demagnetization of basalt by transient stress up to 10 kbar. *J. Geophys.* **41**, 23–41 (1975).
83. N. S. Bezaeva, J. Gattacceca, P. Rochette, R. A. Sadykov, V. I. Trukhin, Demagnetization of terrestrial and extraterrestrial rocks under hydrostatic pressure up to 1.2 GPa. *Phys. Earth Planet. Inter.* **179**, 7–20 (2010).
84. J. Gattacceca, M. Boustie, E. Lima, B. P. Weiss, T. de Resseguier, J. P. Cuq-Lelandais, Unraveling the simultaneous shock magnetization and demagnetization of rocks. *Phys. Earth Planet. Inter.* **182**, 42–49 (2010).
85. W. D. Daily, P. Dyal, Theories for the origin of lunar magnetism. *Phys. Earth Planet. Inter.* **20**, 255–270 (1979).
86. R. J. Reisener, J. I. Goldstein, Ordinary chondrite metallography: Part 2. Formation of zoned and unzoned metal particles in relatively unshocked H, L, and LL chondrites. *Meteorit. Planet. Sci.* **38**, 1679–1696 (2003).
87. L. Kaufman, M. Cohen, The martensitic transformation in the iron-nickel system. *JOM* **8**, 1393–1401 (1956).
88. J. A. Wood, The cooling rates and parent planets of several iron meteorites. *Icarus* **3**, 429–459 (1964).
89. L. J. Swartzendruber, V. P. Itkin, C. B. Alcock, The Fe-Ni (iron-nickel) system. *J. Phase Equilibria* **12**, 288–312 (1991).
90. G. W. Pearce, W. A. Gose, D. W. Strangway, Magnetic studies of Apollo 15 and 16 lunar samples. *Proc. Lunar Planet. Sci. Conf.* **4**, 3045–3076 (1973).
91. C. J. Hale, M. Fuller, R. C. Bailey, On the application of microwave heating to lunar paleointensity determination. *Proc. Lunar Planet. Sci. Conf.* **9**, 3165–3179 (1978).
92. A. Stephenson, Three-axis static alternating field demagnetization of rocks and the identification of natural remanent magnetization, gyroremanent magnetization, and anisotropy. *J. Geophys. Res.* **98**, 373–381 (1993).
93. D. J. Dunlop, Viscous magnetization of 0.04–100 μm magnetites. *Geophys. J. Roy. Astron. Soc.* **74**, 667–687 (1983).
94. E. Thellier, Sur l'aimantation des terres cuites et ses applications géophysiques. *Ann. Inst. Phys. Globe* **16**, 157–302 (1938).
95. S. M. Cisowski, D. W. Collinson, S. K. Runcorn, A. Stephenson, M. Fuller, A review of lunar paleointensity data and implications for the origin of lunar magnetism. *J. Geophys. Res.* **88**, A691–A704 (1983).
96. A. Stephenson, D. W. Collinson, Lunar magnetic field palaeointensities determined by an anhysteretic remanent magnetization method. *Earth Planet. Sci. Lett.* **23**, 220–228 (1974).
97. A. Stephenson, S. K. Runcorn, D. W. Collinson, Paleointensity estimates from lunar samples 10017 and 10020. *Proc. Lunar Planet. Sci. Conf.* **8**, 679–687 (1977).
98. J. Gattacceca, P. Rochette, Toward a robust normalized magnetic paleointensity method applied to meteorites. *Earth Planet. Sci. Lett.* **227**, 377–393 (2004).
99. P. Wasilewski, Magnetization of small iron-nickel spheres. *Phys. Earth Planet. Inter.* **26**, 149–161 (1981).
100. Y. Yu, L. Tauxe, J. S. Gee, A linear field dependence of thermoremanence in low magnetic fields. *Earth Planet. Sci. Lett.* **162**, 244–248 (2007).
101. S.-C. L. L. Lappe, J. M. Feinberg, A. R. Muxworthy, R. J. Harrison, Comparison and calibration of nonheating paleointensity methods: A case study using dusty olivine. *Geochem. Geophys. Geosyst.* **14**, 2143–2158 (2013).
102. Y. Yu, D. J. Dunlop, Ö. Özdemir, Are ARM and TRM analogs? Thellier analysis of ARM and pseudo-Thellier analysis of TRM. *Earth Planet. Sci. Lett.* **205**, 325–336 (2003).
103. R. Shaar, L. Tauxe, Thellier GUI: An integrated tool for analyzing paleointensity data from Thellier-type experiments. *Geochem. Geophy. Geosyst.* **14**, 677–692 (2013).
104. P. Rochette, Magnetic classification of story meteorites: 1. Ordinary chondrites. *Meteorit. Planet. Sci.* **38**, 251–268 (2003).
105. C. R. Pike, A. P. Roberts, K. L. Verosub, Characterizing interactions in fine magnetic particle systems using first order reversal curves. *J. Appl. Phys.* **85**, 6660 (1999).
106. R. Egli, VARIFORC: An optimized protocol for calculating non-regular first-order reversal curve (FORC) diagrams. *Global Planet. Change* **110**, 302–320 (2013).
107. R. J. Harrison, J. M. Feinberg, FORCinel: An improved algorithm for calculating first-order reversal curve distributions using locally weighted regression smoothing. *Geochem. Geophy. Geosyst.* **9**, Q01056 (2008).

108. A. P. Roberts, D. Heslop, X. Zhao, C. R. Pike, Understanding fine magnetic particle systems through use of first-order reversal curve diagrams. *Rev. Geophys.* **52**, 557–602 (2014).
109. S. Cisowski, Interacting vs. non-interacting single domain behavior in natural and synthetic samples. *Phys. Earth Planet. Inter.* **26**, 56–62 (1981).
110. D. J. Dunlop, Ö. Özdemir, *Rock Magnetism: Fundamentals and Frontiers. Cambridge Studies in Magnetism* (Cambridge Univ. Press, 1997), pp. 573.
111. R. Egli, Analysis of the field dependence of remanent magnetization curves. *J. Geophys. Res.* **108**, 2081 (2003).
112. R. A. Sadykov, N. S. Bezaeva, A. I. Kharkovskiy, P. Rochette, J. Gattacceca, V. I. Trukhin, Nonmagnetic high pressure cell for magnetic remanence measurements up to 1.5 GPa in a superconducting quantum interference device magnetometer. *Rev. Sci. Instrum.* **79**, 115102 (2008).
113. D. J. Dunlop, The rock magnetism of fine particles. *Phys. Earth Planet. Inter.* **26**, 1–26 (1981).
114. A. Stephenson, S. Sadikun, D. K. Potter, A theoretical and experimental comparison of the anisotropies of magnetic susceptibility and remanence in rocks and minerals. *Geophys. J. Roy. Astron. Soc.* **84**, 185–200 (1986).
115. G. Turner, ^{40}Ar-^{39}Ar ages from the lunar maria. *Earth Planet. Sci. Lett.* **11**, 169–191 (1971).
116. O. M. Lovera, F. M. Richter, T. M. Harrison, Diffusion domains determined by ^{39}Ar released during step heating. *J. Geophys. Res.* **96**, 2057–2069 (1991).
117. H. Fechtig, S. T. Kalbitzer, The diffusion of argon in potassium-bearing solids, in *Potassium Argon Dating*, O. A. Schaeffer, J. Zähringer, Eds. (Springer-Verlag, 1966), pp. 68–107.
118. S. Huang, Surface temperatures at the nearside of the Moon as a record of the radiation budget of Earth's climate system. *Adv. Space Res.* **41**, 1853–1860 (2008).
119. S. J. Kiehm, K. Peters, M. G. Langseth, J. L. Chute Jr., Apollo 15 measurement of lunar surface brightness temperatures thermal conductivity of the upper 1 1/2 meters of regolith. *Earth Planet. Sci. Lett.* **19**, 337–351 (1973).
120. R. C. Reedy, J. Masarik, Production rates of cosmogenic nuclides deep in the Moon. *Meteoritics* **30**, 564–565 (1995).
121. F. Hörz, E. Schneider, D. E. Gault, J. B. Hartung, D. E. Brownlee, Catastrophic rupture of lunar rocks: A Monte-Carlo simulation. *The Moon* **13**, 235–258 (1975).
122. P. T. Delaney, Heat transfer during emplacement and cooling of mafic dykes, in *Mafic Dyke Swarms*, H. C. Halls, W. Fahrig, Eds. (Geological Association of Canada, 1987), pp. 123–135.
123. M. G. Langseth, S. J. Keihm, K. Peters, Revised lunar heat-flow values. *Proc. Lunar Planet. Sci. Conf.* **7**, 3143–3171 (1976).
124. R. S. Coe, S. Gromme, E. A. Mankinen, Geomagnetic paleointensities from radiocarbon-dated lava flows on Hawaii and the question of the Pacific nondipole low. *J. Geophys. Res.* **83**, 1740–1756 (1978).
125. O. Eugster, T. Michel, Common asteroid break-up events of eucrites, diogenites, and howardites, and cosmic-ray production rates for noble gases in achondrites. *Geochim. Cosmochim. Acta* **59**, 177–199 (1995).

Acknowledgments: We thank M. Fuller for suggesting the study of regolith breccias, J. Gattacceca for sharing pressure remanent magnetization cell, B. Carbone for administrative support, and the Institute for Rock Magnetism at the University of Minnesota for use of their vibrating sample magnetometer. We also thank P. Boehnke and two anonymous reviewers for helpful suggestions. **Funding:** We thank the NASA Solar System Workings and Planetary Major Equipment Programs (grant #NNX15AL62G), the NASA Solar System Exploration Research Virtual Institute node at Brown-MIT (grant #NNA14AB01A), the MIT International Science and Technology Initiatives Global Seed Fund, the Rutgers University School of Arts and Sciences, and the Miller Institute for Basic Research in Science for financial support. **Author contributions:** S.M.T., B.P.W., and D.L.S. conceived the study and supervised the research. S.M.T. designed and carried out the experiments. C.S., H.W., and T.L.G. assisted with the experimental work and analysis. S.M.T. led the writing of the paper with contributions from B.P.W. and D.L.S. **Competing interests:** The authors declare that they have no competing interests. **Data and materials availability:** All data needed to evaluate the conclusions in the paper are present in the paper and/or the Supplementary Materials. Additional data related to this paper may be requested from the authors and will be posted in the Magnetics Information Consortium (MagIC) database (www2.earthref.org/MagIC/).

Submitted 6 February 2017
Accepted 11 July 2017
Published 9 August 2017
10.1126/sciadv.1700207

Citation: S. M. Tikoo, B. P. Weiss, D. L. Shuster, C. Suavet, H. Wang, T. L. Grove, A two-billion-year history for the lunar dynamo. *Sci. Adv.* **3**, e1700207 (2017).

Science Advances

A two-billion-year history for the lunar dynamo

Sonia M. Tikoo, Benjamin P. Weiss, David L. Shuster, Clément Suavet, Huapei Wang and Timothy L. Grove

Sci Adv **3** (8), e1700207.
DOI: 10.1126/sciadv.1700207